Supporting Online Material for

Kinetics of Morphogen Gradient Formation

Anna Kicheva, Periklis Pantazis, Tobias Bollenbach, Yannis Kalaidzidis, Thomas Bittig, Frank Jülicher,* Marcos González-Gaitán*

*To whom correspondence should be addressed. E-mail: julicher@pks.mpg.de (F.J.); marcos.gonzalez@biochem.unige.ch (M.G.-G.)

Published 26 January 2007, *Science* **315**, 521 (2007)
DOI: 10.1126/science.1135774

This PDF file includes

Other Supporting Online Material for this manuscript includes the following:
(available at www.sciencemag.org/cgi/content/full/315/5810/521/DC1)

Contents

1. Materials and methods

Transgenic animals.

shi^{ts1} is described in Flybase. *UAS-GFP-Dpp, UAS-GFP-wingless* and *UAS-Dynamin*$^{+}$ were previously described (*1, 2*). For FRAP experiments the following genotypes were used: 1) *dppGal4*/*UAS-GFP-Dpp* or *dppGal4::UAS-GFP-Dpp*/+ 2) *UAS-GFP-wingless*/+*;dppGal4*/+ 3) *shi*^{ts1}*;UAS-Dynamin*$^{+}$/+*;dpp-gal4*/*UAS-GFP-Dpp* (Dpp "shibire rescue"), and 4) *shi*^{ts1}*;UAS-Dynamin*$^{+}$/*UAS-GFP-wingless; dpp-gal4*/+ (Wg "shibire rescue"). "Shibire rescue" animals were kept at the *shi*^{ts1} permissive temperature (25 ºC or 18 ^{o}C) to allow normal wing development until third instar larva.

Fluorescence Recovery After Photobleaching (FRAP).

Wing imaginal discs were dissected in Clone-8 medium. They were subsequently transferred onto a glass slide into an imaging chamber, made of double sided adhesive tape and filled with 4 µM solution of the membrane dye FM4-64 (Molecular probes) in Cl-8 medium, covered, and sealed with nail polish.

Fluorescence Recovery After Photobleaching (FRAP) experiments were performed on LSM510 laser scanning confocal microscope (Carl Zeiss) with a 40x/1.3 NA Oil Plan-Neofluar objective. GFP was excited with low levels of the 488 nm Argon laser line and GFP emission was detected using a 505-530 nm bandpass filter, using the following settings: laser power 25-50%, transmission 3%, zoom 1.5, pixel time = 1.6 µs, gain ~800, pinhole – 3.34 Airy units (= 2.7 µm optical slice thickness), 8 bit, 0.15 µm × 0.15 µm pixel size. During imaging the samples were maintained at room temperature or heated up approximately 10 minutes prior to bleaching and then maintained at the appropriate temperature with an Objective Heater System (Bioptechs). Before each set of experiments we verified that the sample is heated to the appropriate temperature with

precision of ±0.5 ºC using a custom-made temperature probe inserted in an imaging chamber. For *in vivo* imaging, at each time point a *z*-stack composed of 5 overlapping (2.7 µm thick) confocal sections 1 µm apart from each other was collected, covering the most apical part of the columnar epithelium, where 80±8% (n=11) of the total GFP-Dpp fluorescence and 77±12% (n=6) of the total GFP-Wingless fluorescence is localized *in vivo* (see Figure S1). For quantification, we used a maximum projection of the 5 z-sections for each time point, which allows us to consider the epithelium as a two-dimensional tissue. Time-lapse imaging of the FRAP recovery was performed for approximately one hour at two minutes intervals for GFP-Dpp and one minute intervals for GFP-Wingless.

The fluorescence in the ROI was bleached by performing sets of three bleaching iterations at 3 different *z*-positions with the 488 nm laser line, using 60-80% laser output and 100% transmission. This bleaching procedure results in eliminating 88.5±1.5% (n= 6) of the total fluorescence in the bleached region (for details see section 2 of SOM).

Data analysis.

The fluorescence recovery in the ROI with dimensions 10 µm x 200 µm was quantified by measuring the average fluorescence intensity of the maximum projection for each time point, using the Zeiss LSM software. Background fluorescence was measured in a random region outside the GFP-Dpp receiving tissue. The background, as well as the fluorescence remaining immediately after bleaching (e.g. the bleaching depth) were subtracted (for details on the bleaching depth, see "One-dimensional data analysis"). The average fluorescence intensity was normalized to 1 for the value before bleaching.

The geometry of the ROI is such that the "lateral" contribution of morphogen-GFP molecules in the FRAP experiment is negligible and this reduces the data analysis to a one-dimensional case (Figure S3C,D). Therefore, to estimate the kinetic parameters of morphogen movement D, k, j_0 and ψ from each FRAP recovery curve, we used a one-dimensional solution to equation (1) (see "One-dimensional data analysis", equation (S8)).

The average decay length λ was estimated by fitting an exponential decay function to each individual gradient profile and then taking the average value for each data set. The gradient profiles represent the average fluorescence for each position away from the source and were measured using ImageJ (NIH). λ does not change significantly after incubating the larvae for 1h at 34ºC (Figure S7), therefore we used a constant λ to relate D and k in the FRAP experiments.

The concentration at the source boundary C_0 was estimated by using the fluorescence intensity calibration to measure the average concentration of molecules in the ROI (C_R), and extrapolating the concentration at the source boundary, based on the observation that the gradient is exponential, via:

$$C_0 = \frac{hC_R}{\lambda\left(\exp(-d/\lambda) - \exp(-(d+h)/\lambda)\right)} \tag{6}$$

where h is the width of the ROI, and d is the distance of the ROI to the source (Figure S3).

The cell diameter a = 2.6 μm was estimated from the average area of a cell (5.46±0.82 μm^2, n=1200 cells), assuming that the cell is a circle.

For all values, the mean and the standard deviation are reported, unless otherwise specified.

2. Calibrations and control experiments of the FRAP assay

Before proceeding with the FRAP assay in wing imaginal discs, we first established that five essential conditions (summarized in this section) are fulfilled: 1) most of the GFP-tagged molecules are located in the most apical 5 μm of the epithelium which we image and a basal population does not account for the recovery after bleaching (Figure S1 and S4G,H); 2) the bleaching procedure is not photodamaging the tissue (Figure S2A); 3) photobleaching during the recovery phase is small (Figure S2B); 4) the relationship between fluorescence and concentration is linear (Figure S2C,D); and 5) the range of detection is such that the low levels of GFP-Dpp, which might be diluted in the extracellular space, are detected (Figure S2E-G). In addition, detection of fluorescence intensity was calibrated to GFP-Dpp concentration in our imaging conditions by performing two kinds of assays: 1) using GFP-tagged Rotavirus-like particles (VLPs), each bearing precisely 120 molecules of GFP (*3*), as a calibration standard (Figure S2E-G), and 2) imaging defined concentrations of GFP in solution (Figure S2D).

Using the "VLP" calibration, we also estimated that two standard deviations of the background noise in our imaging conditions are equivalent to about 800 GFP molecules in the ROI (see section 2d and Figure S2E-G). The number of fluorescent molecules in the ROI after photobleaching is in the order of 4.3×10^4 GFP molecules, which implies that we can detect changes of less than 2% for the concentrations of GFP fusion proteins after bleaching. Given this precision of measurement, we asked: is the extracellular pool a major fraction of the GFP-Dpp molecules? To determine the fraction of the extracellular pool, we measured the fraction of the fluorescence associated to the cell profiles counterstained with FM4-64 *in vivo*. This measurement overestimates the extracellular pool size, because it includes the extracellular pool, but also the intracellular GFP-Dpp at the cell cortex. „Extracellular" GFP-Dpp measured this way is equal to or smaller than 15±3.4% (n=8 discs) of the total pool. The latter measurement, together with the fact that our detection inaccuracy is less than 2%, show that the extracellular pool is not a dominant pool.

2a. Apico-basal distribution of fluorescence and bleaching profile.

In the FRAP data analysis the epithelial tissue is viewed as a two dimensional plane (Figure S3), and consequently the process of recovery is considered to occur only at the expense of non-bleached molecules in the territories surrounding the ROI. For the validity of these considerations, two conditions need to be fulfilled: 1) the majority of the fluorescent molecules have to be imaged and projected onto a single plane; 2) the amount of bleaching should be sufficient to eliminate fluorescent molecules throughout the entire depth of the cells, thus making negligible a basal to apical recovery.

Previously it has been observed that the majority of the GFP-Dpp is concentrated in the most apical 5 μm of the wing epithelium (*1*). Therefore, in the FRAP assay we image at the apical side a *z*-stack of 5 overlapping *z*-confocal slices with optical thickness 2.7 μm, which are 1 μm apart, and measure the fluorescence in the maximum projection of the stack. In order to confirm that these imaging conditions indeed capture the majority of the fluorescent molecules, we performed a quantitative analysis of the apico-basal distribution of GFP-Dpp and GFP-Wingless *in vivo*.

For this purpose we imaged *z*-stacks of 30 *z*-confocal slices, 1 μm apart, through the entire depth of the epithelium. The epithelial cells are approximately 30 μm long in the *z*- direction (not shown). Therefore, for quantification we operationally define the total fluorescence in the tissue to be sum of the total fluorescence intensities from each confocal plane in a 30 μm *z*-stack. Our results indicate that *in vivo* 80±8% (n=11) of the total GFP-Dpp, and 77±12% (n=6) of the total GFP-Wingless fluorescence is localized in the top 5 μm of the epithelium in the ROI adjacent to the source (Figure S1C,D), hence most of the fluorescent molecules are represented in the FRAP experiments. Previous reports showed that in fixed discs, extracellular Wg accumulates in the basolateral sides of the cell (*4*). Our *in vivo* quantifications, however, show that a major part of the Wg total pool (intra- plus extracellular) is localized in the most apical 5 μm of the epithelium.

To verify that the bleaching procedure eliminates the fluorescent molecules throughout the entire depth of the tissue, we collected 30 μm *z*-stacks before and immediately after bleaching *in vivo*. The apico-basal distribution of the fluorescence

before and after bleaching (Figure S1A,B) shows that bleaching is very effective in the most apical 10 µm of the tissue, where 92±4% (n=11) of the GFP-Dpp and 87±7% (n=6) of GFP-Wingless is localized (Figure S1C,D). The quantitative analysis shows that 11.5±1.5% (n=5) of the total GFP-Dpp and 14±9% (n=6) of the total GFP-Wingless fluorescence remains after bleaching (Figure S1A-D). This value is an overestimate of the actual remaining fluorescence after bleaching ("bleaching depth"), since the analysis is carried out *in vivo* and some recovery has occurred during bleaching and during the time of post-bleach image acquisition. Therefore, the actual bleaching depth is smaller than 11.5±1.5%, but strictly is experimentally unknown, which is accounted for in the data analysis procedure (see "Data analysis"). Analysis of the recovery in the 5 separate sections of the *z*-stack shows no indication of faster or stronger fluorescence recovery in the more basal sections compared to the more apical ones (not shown). In summary, the bleaching procedure used in the FRAP experiments eliminates most of the fluorescence along the entire depth of the tissue in the ROI and the observed FRAP recoveries cannot be attributed to movement of non-bleached basal molecules to the apical side of the cell.

In order to exclude the possibility that we are underestimating the amount of total fluorescence due to decreased light penetration deeper in the tissue, which would lead to an underestimation of the number of molecules in the basal side, we studied the optical light penetration effect in the wing epithelium. For this reason, we expressed and imaged cytosolic GFP, which is evenly distributed throughout the whole cell, in particular along the complete apico-basal axis. Based on this, a "*z*-calibration" curve was obtained by measuring the fluorescence intensity of cytosolic GFP as a function of the *z* position normalized to the fluorescence in the apical end. Then the apico-basal fluorescence distribution of GFP-Dpp was normalized to this *z*-calibration curve (Figure S1E). The resulting normalized distribution of fluorescence is very similar to the non-normalized distribution for the first 25 µm of the tissue (Figure S1E). However, most basally the penetration is close to zero, which indicates that there might be basally localized molecules which are undetectable.

To check if such a basal population exists, we embedded the discs in an imaging chamber made of 2 coverslips separated by thin spacers, which forces the discs to flatten

and exposes the basal side of the tissue close to a coverslip. Discs embedded this way can be imaged from both sides, and the fluorescence profile can be reconstructed completely by concatenating the apico-basal and baso-apical *z*-stacks of the same disc (Figure S1F). With this analysis a small punctate basal population of GFP-Dpp was observed, which constitutes 19.3±5.2% (n=4) of the total fluorescence. To verify that this basal pool is not a source of recovery, we performed time-lapse imaging of basally embedded discs to determine whether this basal population tends to apicalize during incubation. Our results show that the basal population of molecules is very stable and does not move apically during the period of incubation (not shown). Therefore, the existence of this basal pool does not affect the quantitative analysis of the FRAP experiments.

Finally, we performed a modified FRAP experiment, in which a 30 μm × 30 μm square was bleached next to the source, to verify that indeed the observed fluorescence recovery occurs by movement of molecules from the neighboring non-bleached areas (Figure S4G). The bigger size of the ROI in this case allows observing the recovery of fluorescence first at the edges of the ROI and with some delay in the middle. Indeed, quantification of the center of the bleached region (a 10 μm × 10 μm square, see Figure S4G) shows that the recovery is in good agreement with the theoretical curve, describing such a difference in the recovery kinetics compared to the recovery of the whole 30 μm square (Figure S4H). If recovery occurs due to movement of basal molecules to the apical side, the recovery curves would look identical. Therefore, it can be confidently concluded that the fluorescence recoveries observed in the FRAP experiments occur at the expense of non-bleached molecules from the areas surrounding the ROI.

2b. Effect of bleaching on the tissue.

In order to test whether bleaching impairs the cellular machineries responsible for the observed recoveries, we performed an experiment in which the same ROI was bleached once, left to recover for 1000 seconds, then bleached a second time and left to recover for a further 1500 seconds. The shape of the recovery curves and the corresponding mobile fractions observed after the two bleaching events are similar (Figure S2A). This result demonstrates that bleaching does not hamper the trafficking of

the fluorescently labeled molecules. The fact that the recoveries of GFP-Wingless at 25 ºC are almost complete (Figure 3J), as well as the reversible nature of the shibire block (Figure S8), further support this conclusion.

In addition, we have observed that during the FRAP experiments, the tissue does not show signs of damage caused by cytotoxicity of the bleaching procedure. In some cases, damage can be recognized by 1) abnormal intense fluorescence of the FM4-64 dye beyond the plasma membrane staining which often occurs upon strong illumination with ultraviolet light, or 2) complete lack of molecule movement. We have also confirmed that the permeability barrier of the cells is intact by using the vital dye acridine orange (not shown).

2c. Fluorescence intensity and concentration are linearly related.

The proper interpretation of the FRAP experiments requires that average fluorescence intensity of the GFP-morphogen fusion can be used as measure of the concentration of these molecules. Therefore, we set our imaging conditions in such a way, that the detected amounts of fluorescence are linearly related to concentrations of molecules. To verify this "linearity condition" of our imaging setup, we utilized two different experimental approaches: 1) a stepwise bleaching assay and 2) calibration of the fluorescence/concentration relationship by using defined solutions of recombinant GFP.

Stepwise bleaching

The stepwise bleaching assay to verify the linear relationship between concentration and fluorescence intensity is based on the fact that photobleaching exerted with a defined illumination intensity eliminates the fluorescence of a constant fraction of the GFP molecules. The concentration of molecules after n number of bleaching steps is

$$c_n = \phi^n c_0, \tag{S1}$$

where ϕ is the bleached fraction of molecules per step with a defined intensity of illumination and c_0 the initial concentration. From equation (S1) it follows that the logarithm of the concentration is linearly related to the number of bleaching steps n:

$$\ln c_n = \ln\left(\phi^n c_0\right) = n\ln\phi + \ln c_0. \quad \text{(S2)}$$

If concentration and fluorescence are linearly related, then

$$c = \gamma \cdot I, \quad \text{(S3)}$$

where γ [(molecules × pixel)/(counts × μm^2)] is the conversion factor between the average fluorescence intensity in the ROI I [counts/pixel] and the concentration c [molecules/μm^2]. Plugging (S3) into (S2):

$$\ln(I_n) = n\ln\phi + \ln I_0. \quad \text{(S4)}$$

Therefore if concentration and fluorescence intensity are linearly related, upon stepwise bleaching the logarithm of the intensity is also linearly related to the number of bleaching steps *n.* Indeed equation (S3) is the only one that satisfies equation (S4).

In a given ROI, we performed a series of up to 6 bleaching steps in GFP-Dpp or GFP-Wingless expressing discs (Figure S2C). The average fluorescence in the bleached region was measured after each bleaching step and the background was subtracted. We observed that dependence between the logarithm of the measured I and the number of bleaching steps is well described by a linear relationship. This indicates that intensity and concentration are proportional in our conditions of imaging GFP-Dpp and GFP-Wingless.

GFP in solution

GST tagged GFP (GST-GFP) was expressed in *E. Coli* and purified according to a standard protocol (Amersham Biosciences). Solutions with different concentration of recombinant GFP in Clone 8 medium were imaged in the same imaging conditions as the FRAP experiments. Single *z*-sections (see methods) were used to measure the average fluorescence corresponding to each concentration. The number of GFP molecules corresponding to each GFP concentration was calculated from the sample volume imaged. The sample volume was estimated from the dimensions of imaged ROI and the thickness of the optical slice using the algorithm in the Zeiss LSM 510 software (Carl Zeiss LSM handbook). The resulting curve relating the number of GFP molecules to

fluorescence intensity (Figure S2D) shows that below average fluorescence of ~200 counts/pixel the relationship between concentration and fluorescence intensity is linear. The average fluorescence intensity in the ROI (10 μm wide stripe next to the source) in the GFP-Dpp and GFP-Wingless expressing wing discs is below 100 counts, indicating that imaging in the FRAP experiments was performed within the linear range of detection.

2d. Range of detection.

Once we determined that we are imaging the GFP fusions linearly, we established the range where GFP concentration can be detected in a linear regime and above the noise level in the ROI. To address this, we performed an assay using rotavirus-like particles (VLPs), tagged with exactly 120 GFP molecules per particle (*3*), to calibrate the fluorescence intensity and determine the noise level which limits detection at lower concentrations (see also (*5, 6*)).

A small drop (~ 5 μl) of 7 μg/ml GFP-VLP solution was suspended in Mowiol mounting medium to immobilize the particles and imaged under identical imaging conditions as the FRAP experiments. Sets of images were collected and fluorescent structures were automatically recognized and modeled using the Motion Tracking II program as described in Rink et al (*6*). The VLP particles have a sub-resolution size and in confocal microscopy they appear as point sources with a characteristic point spread function over a few pixels (1 pixel = 0.15 × 0.15 μm^2). To estimate the number of photons coming from a detected particle during imaging, we integrate the fluorescence intensity over the apparent fluorescent spot. The integrated fluorescence intensities of 8733 spots were determined (Figure S2E,F). The experimental distribution $\rho(I)$ of the fluorescence intensities I [cnts/spot] was fitted by a sum of Gaussians:

$$\rho(I) = \sum_{i=1}^{N} \frac{A_i}{\sqrt{2\pi}\sigma_i} \exp\left(-\frac{(I-\mu_i)^2}{2\sigma_i^2}\right), \qquad \text{(S5)}$$

where μ_i is the mean, σ_i the standard deviation, A_i the amplitude, and N the number of Gaussians. μ_i, σ_i, and A_i are fit parameters. The optimal number of Gaussians N=4 was

determined by a probabilistic procedure as described previously (*7*). The residual of the fit is $\chi^2_{n=87} = 107.2$ for our number of bins n=87. The $\chi^2_{n=87}$ below 109.8 is within 95% confidence interval indicating very good agreement between the experimental data and the theoretical sum of Gaussians. The mean values μ_i of the integrated spot intensity for each Gaussian are integer multiples $\mu_i = i \cdot \mu$. The deviation from the integer factors is within the estimated error bars ($\mu_1/\mu = 1 \pm 0.04$, $\mu_2/\mu = 1.83 \pm 0.17$, $\mu_3/\mu = 3.17 \pm 0.54$). This indicates that the first and major peak corresponds to a single VLP containing 120 GFP molecules, the second peak, to aggregates of two VLPs and so on. The single virus particle peak corresponds to an integrated intensity of 1238±45 counts/VLP. Since the virus capsid contains 120 GFP molecules, the total intensity of one GFP molecule is 10.3±0.4 counts.

To study what is the minimum density of GFP molecules which can be reliably detected, we estimated the fluctuations of fluorescence intensity in our images. During fluorescent imaging, the main type of noise has a Poisson distribution. This can be described by the mean intensity

$$\langle I \rangle = \alpha \langle N \rangle + \beta, \tag{S6}$$

and the variance of intensity

$$D(I) = \alpha^2 \langle N \rangle = \alpha(\langle I \rangle - \beta) = \alpha \langle I \rangle - \alpha\beta, \tag{S7}$$

where α is the number of counts per photon, $\langle N \rangle$ is the mean number of photons, $D(I)$ is the variance for each intensity level $\langle I \rangle$, β is the offset level of the microscope (i.e. the estimated number of counts in the image in the absence of light).

The best way to measure the mean intensity $\langle I \rangle$ and variance of intensity $D(I)$ of a given pixel is acquiring a time sequence, which would give a series of counts for this pixel. In this case, calculation of the mean value and the variance for a given pixel is straightforward. In the case of still images, the mean value $\langle I \rangle$ and variance $D(I)$ of intensity could be estimated as the average of I and $(I-\langle I \rangle)^2$ respectively within the small 3×3 pixels vicinity of a given pixel. The spatial approximation is acceptable in regions of low intensity. This approach was tested by comparison of variance/intensity dependence

calculated from time series in the straightforward way and in the spatial approximation way. The result of the two calculations is similar (data not shown).

To determine α and β, $D(I)$ and $\langle I \rangle$ were estimated in the vicinity of each pixel (3×3 pixels). For any value of $\langle I \rangle$, the mean value of the corresponding variances $D(I)$ was plotted for low intensity values (Figure S2G). The resulting data fits well to the linear equation (S7) with correlation index $R^2 = 0.997$, where $\alpha = 38.1 \pm 0.5$ counts/photon and $\alpha\beta = 79 \pm 9$ counts^2/photon. Therefore, the offset β is 2.07±0.23 counts.

We are measuring the fluorescence in a ROI with dimensions of 10 μm × 200 μm (corresponding to 89×10^3 pixels). In this ROI, we estimated experimentally the integrated autofluorescence which is about 4.5×10^5 counts corresponding to about 1.18×10^4 photons (4.5×10^5 counts/(38.1 counts/photon)). In the FRAP experiments the integrated intensity in the ROI before bleaching is approximately 6.7×10^6 counts and immediately after bleaching approximately 4.5×10^5 counts after subtraction of the autofluorescent background. The precision of this background subtraction can be estimated by considering the standard deviation of the autofluorescence Poisson noise, which is 109 photons (standard deviation $SD(I) = \sqrt{D(I)} = \sqrt{1.18 \times 10^4}$ photons $= 109$ photons), equal to 4.1×10^3 counts (109 photons × 38.1 counts/photon). Therefore, the error of background subtraction is about $2 \times SD \approx 8000$ counts. This implies that in the "dimmest" images (after bleaching), the detected signal is about 55 times (i.e. 98% of the total; cf. 8000 vs. 4.5×10^5) above two standard deviations of the autofluorescence noise. As recovery occurs and more molecules enter the ROI, the GFP signal to autofluorescence noise ratio improves and almost 100% of the fluorescent molecules can be detected above the level of autofluorescence noise at the plateau phase of recovery.

3. Modified FRAP assays

In order to test the validity of the diffusion and degradation description for the FRAP recoveries, we performed FRAP experiments in different geometries, such as different ROI shapes and measurements at different distances from the source. We find

that the calculated recovery curves for all situations considered are still in good agreement with the experimental data and they yield similar values for *D, k,* ν and ψ (Figure S4 and Table S1). In these experiments, the ROI width is increased to 20 µm (Figure S4A,B) or is located 20 µm away, instead of adjacent to the source (Figure S4C,D). Alternatively, the ROI is located perpendicularly instead of parallel to the source ("perpendicular FRAP"; Figure S4E,F). In yet another assay, a 30 µm × 30 µm square was bleached next to the source (Figure S4G,H) and two different regions embedded within each other are considered. The results of these experiments furthermore are consistent with the independence of the four kinetic parameters on position in the tissue (see also section 6)

4. Diffusion equation with degradation and production

Equation (1) with $k = 0$ and $j_0 = 0$ is the well known diffusion equation which describes non-directional transport processes (*8*). Here it describes the time-dependent concentration of morphogens. The fact that morphogens are produced in a localized source, is described in equation (1) by a production term $2j_0\delta(x)$, which corresponds to a line source located at $x = 0$, where $\delta(x) = 0$ for $x \neq 0$ and $\int_{-\infty}^{\infty} dx\delta(x) = 1$. This localized production leads to a morphogen current $-D\partial_x C = j_0$ at $x = 0$. The degradation of morphogens occurs in the tissue at a rate k.

In steady state, the concentration profile by definition does not change with time, i.e. $\partial_t C = 0$ in (1). To verify that equation (2) is indeed the steady state solution for $x > 0$, we insert $C(x) = C_0 e^{-\frac{x}{\lambda}}$ into equation (1) for $\partial_t C = 0$. This leads to the relation $\frac{D}{\lambda^2} C(x) - kC(x) = 0$, implying $\lambda = \sqrt{D/k}$, which is equation (3). The morphogen current j_0 at $x = 0$ and the concentration C_0 at $x = 0$ in steady state are related by:

$j_0 = -D\partial_x C\big|_{x=0} = -D\partial_x C_0 e^{-\frac{x}{\lambda}}\Big|_{x=0} = \frac{D}{\lambda}C_0 = C_0\sqrt{Dk}$ which is equation (4). Similar analysis has been carried out in previous reports (*9-13*).

5. One-dimensional data analysis

As described in Materials and methods and Figure S3A, during image acquisition in the FRAP experiments *z*-stacks composed of 5 optical sections in the apical part of the epithelium are collected. For quantification a maximum projection of the 5 sections in each *z*-stack is used, which allows treating the epithelial tissue as a two-dimensional plane. In addition, in all experiments where the ROI is parallel to the source ("parallel" FRAP), contribution to fluorescence recovery from the shorter lateral sides of the ROI is negligible, which further reduces the analysis to a one dimensional geometry (Figure S3B,C).

Therefore, to estimate the kinetic parameters of morphogen movement D, k, ψ , j_0, we calculated a one-dimensional solution $C(x,t)$ of equation (1) which corresponds to a parallel FRAP experiment. As initial condition at time t=0, we imposed the steady state profile $C(x,t=0) = C_0 e^{-\frac{x}{\lambda}}$ outside of the bleached region for $x<d$ and $x>d+h$, and $C(x,t=0) = bC_0 e^{-\frac{x}{\lambda}}$ inside the bleached region for $d<x<d+h$, where d is the distance of the ROI to the source, h is the width of the ROI and b is the bleaching depth (also see below).

The analytical solution of this problem is

$$C(x,t) = \frac{(1-\psi)C_0}{2} e^{-x/\lambda}\left[1+b+(b-1)\left(-A(-x,t)+e^{2x/\lambda}\left(-A(x,t)+A(h+x,t)\right)-1+A(h-x,t)\right)\right]+C_\psi(x) \quad \text{(S8)}$$

where $A(x,t) = \mathrm{erf}\left(\frac{d+2Dt/\lambda+x}{2\sqrt{Dt}}\right)$ with the error function $\mathrm{erf(z)} = \frac{2}{\sqrt{\pi}}\int_0^z \exp(-q^2)dq$, and $C_\psi(x)$ represents the concentration of immobile molecules that is constant in time:

$C_\psi(x) = \psi C_0 e^{-x/\lambda}$ outside of the bleached region and $C_\psi(x) = b\psi C_0 e^{-x/\lambda}$ inside the bleached region. The kinetic parameters are D and ψ, and the parameter describing the bleaching is b.

From the solution (S8), we calculated the recovery of the average concentration $f(t)$ in the bleached region $f(t) = \frac{1}{h}\int_d^{d+h} dx' C(x',t)$ (see (F1) in "Supplementary equations" for the explicit expression for $f(t)$; theoretical time development of the concentration recovery is represented in Figure S3D). In the fitting procedure the experimentally known parameters are the gradient profile parameters (C_0 and λ), and the ROI parameters (d and h). The kinetic parameters D and ψ are variable. The corresponding degradation rate k is determined from λ and D using equation (3).

The solution (S8) corresponds to a situation where bleaching occurs instantaneously. In reality, bleaching takes about 45 s and there is a small time lag (10-25 s) between the end of bleaching and the acquiring of the first post-bleach image. The solution corresponding to a finite bleaching time can only be calculated numerically, which would technically complicate the analysis. Therefore, we assume that bleaching occurs instantaneously 25 s before start of imaging. We have verified that our results do not depend sensitively on the choice of this time between 10 s and 70 s. In addition, because there is some recovery of fluorescence during both bleaching and the first post-bleach image acquisition, the value of b is experimentally unknown and therefore this parameter is optimized in the fitting procedure.

To further validate this fitting procedure, we have numerically calculated solutions of equation (1) that take the time needed for bleaching into account. Analogously to the experiments, we generated simulated FRAP recovery curves, consisting of time points at 180 s intervals. We analyzed this numerical data using the fitting procedure described above in order to verify that our analysis is able to return the correct input values of the parameters. The parameters obtained from the fit were at most 15% different from the ones that were used in the numerical solution. This implies that

the finite bleaching time, the time intervals of imaging, and the duration of measurement do not significantly distort the estimation of the kinetic parameters.

It is worth noting that fitting a solution of the diffusion equation without degradation and production terms (Axelrod et al. (*14*) modified for a stripe, not shown) to these simulated recovery curves yields parameter values that deviate substantially from the input parameters (by up to a factor of three). We have also confirmed that the diffusion equation alone is not in agreement with our experimental data (not shown). This indicates that diffusion alone is inadequate to account for FRAP recoveries which are affected by the processes of production and degradation.

6. Two-dimensional data analysis

"Perpendicular" FRAP

To validate the values of the obtained kinetic parameters and as a control of the theory underlying the FRAP data analysis, we devised a modified FRAP assay ("perpendicular" FRAP) where a 10 µm wide stripe is bleached perpendicularly to the source (Figures S3D and S4E). Quantification of the fluorescence recovery in the "perpendicular" FRAP assay involves dividing the bleached stripe into squares of 10 µm width (Figure S4E,F) and measuring the average fluorescence intensity in each square. In this case the lateral contribution to the fluorescence recovery cannot be ignored and the one-dimensional description of the recovery process is not adequate. Therefore, we calculated a two-dimensional solution of equation (1). As initial condition, we used the steady state profile $C(x,y,t=0) = C_0 e^{-\frac{x}{\lambda}}$ outside of the bleached region ($-h/2 < y < h/2$) and $C(x,y,t=0) = bC_0 e^{-\frac{x}{\lambda}}$ inside this region. The analytical solution of this problem is

$$C(x,y,t) = \frac{(1-\psi)C_0}{4} e^{-x/\lambda}[2\left(1 - B_-(x,t) - e^{2x/\lambda}(1 - B_+(x,t))\right) + \left(1 + B_-(x,t) + e^{\frac{2x}{\lambda}}(1 - B_+(x,t))\right) \times\left((b-1)(G(-y,t) + G(y,t)) + 2\right)] + C_\psi(x,y) \quad \text{(S9)}$$

where $B_{\pm}(x,t) = \mathrm{erf}\left(\frac{\pm 2Dt/\lambda + x}{2\sqrt{Dt}}\right)$, $G(y,t) = \mathrm{erf}\left(\frac{h+2y}{4\sqrt{Dt}}\right)$, and $C_{\psi}(x,y)$ represents the concentration of immobile molecules that is constant in time: $C_{\psi}(x,y) = \psi C_0 e^{-x/\lambda}$ outside of the bleached region and $C_{\psi}(x,y) = b\psi C_0 e^{-x/\lambda}$ inside the bleached region. From this we calculated the recovery of the average concentration $f_d(t)$ in the different squares inside the bleached region in which we analyzed the fluorescence recovery separately via $f_d(t) = \frac{1}{h^2}\int_{-h/2}^{h/2} dy' \int_{d}^{d+h} dx' C(x',y',t)$ where d is the distance of the analyzed sub-region from the source (d = 2 µm, 12 µm, 22 µm, 32 µm) and h = 10 µm (see (F2) in "Supplementary equations" for the explicit expression for $f_d(t)$; theoretical time development of the concentration recovery in a „perpendicular" FRAP experiment is represented in Figure S3F-I). We then performed a simultaneous fit of the functions $f_d(t)$ to the measured recovery in the corresponding regions using D, k, ψ and b as free parameters. Imposing that the fluorescence recovery takes place with the same kinetics at different distances to the source, i.e. the recovery curves in all squares have to fit the same parameters, serves as an internal constraint on D, k, j_0 and ψ during the fitting procedure. Using this method, it is not necessary to use the constraint $k=D/\lambda^2$ and independent values for D and k are obtained, which are consistent with the experimentally determined λ. The resulting values for D, k, j_0 and ψ are very similar to the values obtained by parallel FRAP, indicating that the parallel FRAP assay (which relies on the constraint $\lambda = \sqrt{D/k}$) already provides an accurate determination of the kinetic parameters of morphogen spreading and the data analysis procedure is reliable.

It is worth noting that the fitting is consistent with values of D and k do not change at different distances from the source. However, it is possible that there is a weak dependence on position which might be hidden in the imprecision of the parameter determination. It is also likely that the concentrations in the target tissue are in a regime, where non-linearities which lead to a position dependence of parameters are not important (see Bollenbach et al. (*9*)).

30 µm × 30 µm square FRAP

In this modified FRAP assay (Figure S4G,H), a square region of 30 µm width is bleached. The bigger width of the ROI allows us to measure the recovery profiles of two nested square regions inside the ROI (total ROI 30 µm x 30 µm square, and center ROI 10 µm x 10 µm square, see Figure S4G). The corresponding theoretical curves show a qualitative difference between the recoveries in the nested regions, which is confirmed by the experimental data (Figure S4H). This indicates that theory attributing the recoveries to diffusion plus degradation of molecules from the neighboring non-bleached areas is accurate. In addition, this experiment demonstrates that the observed recoveries cannot be ascribed to movement of basal molecules to the apical side of the cell (see also "Apico-basal distribution of fluorescence and bleaching profile").

The analytical solution for the concentration profile when the bleached region is a square of width h at distance d from the source (i.e. the region $d < x < d + h$, $-h/2 < y < h/2$) is:

$$\begin{aligned} C(x,y,t) &= \frac{(1-\psi)C_0}{4} e^{-x/\lambda}[4-(b-1)\big(G_-(y,t)+G_+(y,t)\big) \\ &\times\Big(A(-x,t)-A(h-x,t)+e^{2x/\lambda}\big(A(x,t)-A(h+x,t)\big)\Big)] + C_\psi(x,y) \end{aligned} \quad , \tag{S10}$$

where $A(x,t) = \mathrm{erf}\left(\frac{d+2Dt/\lambda+x}{2\sqrt{Dt}}\right)$, $G_\pm(y,t) = \mathrm{erf}\left(\frac{h\pm 2y}{4\sqrt{Dt}}\right)$, and $C_\psi(x,y)$ represents the concentration of immobile molecules that is constant in time: $C_\psi(x,y) = \psi C_0 e^{-x/\lambda}$ outside of the bleached region and $C_\psi(x,y) = b\psi C_0 e^{-x/\lambda}$ inside the bleached region. From this we calculated the average concentration in the total ROI $f(t) = \frac{1}{h^2}\int_{-h/2}^{h/2} dy' \int_d^{d+h} dx' C(x',y',t)$ and in the centre ROI of width $h/3$ $f_{\mathrm{center}}(t) = \frac{1}{(h/3)^2}\int_{-h/6}^{h/6} dy' \int_{d+h/3}^{d+2h/3} dx' C(x',y',t)$ (see (F3) and (F4) in "Supplementary equations" for the explicit expressions for $f(t)$ and $f_{\mathrm{center}}(t)$ respectively). Both functions were simultaneously fitted to the recovery data as described above. We used a fixed decay length $\lambda = 20\mu\mathrm{m}$ in these fits.

7. “Shibire rescue” assays

Previously we have shown that spreading of Dpp depends on Dynamin-mediated endocytosis, by using animals where the target tissue is mutant for the thermosensitive *shibire*^{ts1} allele (*15*) and the source is rescued by a functional *shibire*$^{+}$ transgene („shibire rescue“ animals; see Materials and methods and (*1*)). However, it was not possible to distinguish whether endocytosis affects the rate of Dpp diffusion, its degradation or the size of the immobile fraction. In previous reports, in the „shibire rescue“ experiments (*1*), the normal steady-state distribution of GFP-Dpp shifts over a period of 6 to 8 hours to a new steady-state of reduced Dpp range. This happens because the spreading of the ligand is challenged by the *shibire*^{ts1} mutant receiving territory at the restrictive temperature. Therefore, capturing the effect of endocytosis loss on the Dpp gradient was only possible after long incubations at the non-physiological restrictive temperature in cells that do not perform endocytosis. The FRAP assay addresses these shortcomings and allows us to determine separately D, k, ν and ψ in each experimental condition and for only a few minutes during the FRAP experiment.

In addition, the FRAP assay allows us to measure sensitively the kinetic effects in conditions of partial and complete endocytic block. In previous “shibire rescue” experiments in which endocytosis is not completely blocked, partial loss of endocytosis did not seem to cause a qualitative effect on the Dpp range (*16*) (Figure S5). In this regard, we asked what is the extent of endocytosis block at different temperatures in the wing imaginal disc. In a number of previous reports, it has been established that *shi*^{ts1} mutant presynaptic terminals of the Drosophila Neuromuscular junction show a complete block of endocytosis at 29 ˚C (*17, 18*). However, in a previous report (*1*) we found that 29 ˚C and 32 ˚C do not cause a complete block of endocytosis in *shi*^{ts1} mutant third instar wing imaginal disc (see also Fig. S5A-L). Complete endocytic block only occurs at 34˚C (Fig. S5M-R.). In a recent report (*16*), some of our experiments addressing the role of endocytosis during the formation of the Dpp gradient (*1*) were repeated by blocking endocytosis with *shi*^{ts1} at 32 ˚C instead of 34 ˚C. This difference in temperature (as well as differences in the temperature used to activate via Gal4 the expression of GFP-Dpp)

explains why the results obtained in the two cases and therefore the conclusions about the requirement of endocytosis during Dpp spreading are different.

8. Reversible endocytosis block

In order to confirm that the lack of recovery in the case of Dpp "shibire rescue" at the fully restrictive temperature of 34 ºC is not due to unspecific tissue damage, we verified that the tissue has retained its ability to transport GFP-Dpp at the permissive temperature after a period of incubation at 34 ºC. For this reason we performed a FRAP experiment in which the "shibire rescue" discs were initially shifted to the restrictive temperature, allowed to warm for about 10 minutes, photobleached and imaged for approximately 10 minutes at 34 ºC. Subsequently the sample was gradually (within 5 minutes) cooled down to the permissive temperature of 25 °C and fluorescence recovery was observed in the ROI (Figure S8). The incubation times were chosen this way, so that the total duration of the experiment does not exceed 60 minutes, as typically done in our FRAP assays.

9. Supplementary equations

Parameters:

t – time

D – diffusion coefficient

ψ – immobile fraction

λ – decay length

C_0 – concentration at the source boundary

d – distance of the ROI to the source

h – ROI width

b – bleaching depth

One dimension:

$$
\begin{aligned}
f(t) \quad = \quad & \frac{C_0}{2h}\Bigg[e^{-\frac{d+h}{\lambda}}(e^{h/\lambda}\lambda(b+(b-1)\psi+1)-2\lambda((b-1)\psi+1)) \\
& +(b-1)e^{-\frac{Dt+(d+h)\lambda}{\lambda^2}}\lambda(\psi-1)\Bigg(e^{h/\lambda}\mathrm{erf}\Big(\frac{d}{\sqrt{Dt}}\Big)+e^{\frac{Dt+h\lambda}{\lambda^2}}-e^{h/\lambda}\mathrm{erf}\Big(\frac{h}{2\sqrt{Dt}}\Big)+\mathrm{erf}\Big(\frac{h}{2\sqrt{Dt}}\Big) \\
& +\mathrm{erf}\Big(\frac{d+h}{\sqrt{Dt}}\Big)-e^{h/\lambda}\mathrm{erf}\Big(\frac{2d+h}{2\sqrt{Dt}}\Big)+e^{\frac{Dt}{\lambda^2}}\mathrm{erf}\Big(\frac{\sqrt{Dt}}{\lambda}\Big)+e^{\frac{Dt+h\lambda}{\lambda^2}}\mathrm{erf}\Big(\frac{\sqrt{Dt}}{\lambda}\Big)+e^{\frac{Dt}{\lambda^2}}\mathrm{erf}\Big(\frac{h\lambda-2Dt}{2\sqrt{Dt}\lambda}\Big) \\
& -e^{\frac{Dt+h\lambda}{\lambda^2}}\mathrm{erf}\Big(\frac{2Dt+h\lambda}{2\sqrt{Dt}\lambda}\Big)+e^{\frac{Dt+2d\lambda+h\lambda}{\lambda^2}}(-\mathrm{erf}\Big(\frac{Dt+d\lambda}{\sqrt{Dt}\lambda}\Big)-e^{h/\lambda}\mathrm{erf}\Big(\frac{Dt+(d+h)\lambda}{\sqrt{Dt}\lambda}\Big) \\
& +(1+e^{h/\lambda})\mathrm{erf}\Big(\frac{2Dt+(2d+h)\lambda}{2\sqrt{Dt}\lambda}\Big))-\mathrm{erf}\Big(\frac{2d+h}{2\sqrt{Dt}}\Big)\Bigg)\Bigg] \qquad \text{(F1)}
\end{aligned}
$$

Two dimensions, perpendicular FRAP, with $\mathrm{erfc}(z)=1-\mathrm{erf}(z)$:

$$
\begin{aligned}
f_d(t) \quad = \quad & \frac{C_0}{4h^2}\Bigg[-2e^{-\frac{d+h}{\lambda}}(-1+e^{h/\lambda})h\lambda(\psi-1)-2e^{-\frac{Dt+(d+h)\lambda}{\lambda^2}}h\lambda\Bigg(e^{\frac{d+h}{\lambda}}\mathrm{erf}\Big(\frac{d}{2\sqrt{Dt}}\Big)-e^{\frac{d+h}{\lambda}}\mathrm{erf}\Big(\frac{d+h}{2\sqrt{Dt}}\Big) \\
& +e^{\frac{Dt}{\lambda^2}}\Big(\mathrm{erf}\Big(\frac{(d+h)\lambda-2Dt}{2\sqrt{Dt}\lambda}\Big)-e^{h/\lambda}\mathrm{erf}\Big(\frac{d\lambda-2Dt}{2\sqrt{Dt}\lambda}\Big)\Big)\Bigg)(\psi-1) \\
& +\frac{1}{\sqrt{\pi}}\Bigg(2e^{-\frac{h^2}{4Dt}-\frac{d+h}{\lambda}-\frac{Dt}{\lambda^2}}\lambda\Big(e^{\frac{d+h}{\lambda}}\mathrm{erf}\Big(\frac{d}{2\sqrt{Dt}}\Big)-e^{\frac{d+h}{\lambda}}\mathrm{erf}\Big(\frac{d+h}{2\sqrt{Dt}}\Big)+e^{\frac{Dt}{\lambda^2}}\Big(\mathrm{erf}\Big(\frac{(d+h)\lambda-2Dt}{2\sqrt{Dt}\lambda}\Big) \\
& -e^{h/\lambda}\mathrm{erf}\Big(\frac{d\lambda-2Dt}{2\sqrt{Dt}\lambda}\Big)\Big)\Big)\Big(-2(b-1)\sqrt{Dt}(-1+e^{\frac{h^2}{4Dt}})+be^{\frac{h^2}{4Dt}}h\sqrt{\pi}\mathrm{erf}\Big(\frac{h}{2\sqrt{Dt}}\Big) \\
& +e^{\frac{h^2}{4Dt}}h\sqrt{\pi}\mathrm{erfc}\Big(\frac{h}{2\sqrt{Dt}}\Big)\Big)(\psi-1)\Bigg)-2e^{-\frac{Dt}{\lambda^2}}h\lambda\Big(\mathrm{erf}\Big(\frac{d}{2\sqrt{Dt}}\Big)-\mathrm{erf}\Big(\frac{d+h}{2\sqrt{Dt}}\Big)+e^{\frac{Dt+d\lambda}{\lambda^2}}\Big(\mathrm{erfc}\Big(\frac{2Dt+d\lambda}{2\sqrt{Dt}\lambda}\Big) \\
& -e^{h/\lambda}\mathrm{erfc}\Big(\frac{2Dt+(d+h)\lambda}{2\sqrt{Dt}\lambda}\Big)\Big)\Big)(\psi-1)+\frac{1}{\sqrt{\pi}}(2e^{-\frac{h^2}{4Dt}-\frac{Dt}{\lambda^2}}\lambda\Big(-2(b-1)\sqrt{Dt}(-1+e^{\frac{h^2}{4Dt}}) \\
& +be^{\frac{h^2}{4Dt}}h\sqrt{\pi}\mathrm{erf}\Big(\frac{h}{2\sqrt{Dt}}\Big)+e^{\frac{h^2}{4Dt}}h\sqrt{\pi}\mathrm{erfc}\Big(\frac{h}{2\sqrt{Dt}}\Big)\Big)\Big(\mathrm{erf}\Big(\frac{d}{2\sqrt{Dt}}\Big)-\mathrm{erf}\Big(\frac{d+h}{2\sqrt{Dt}}\Big) \\
& +e^{\frac{Dt+d\lambda}{\lambda^2}}\Big(\mathrm{erfc}\Big(\frac{2Dt+d\lambda}{2\sqrt{Dt}\lambda}\Big)-e^{h/\lambda}\mathrm{erfc}\Big(\frac{2Dt+(d+h)\lambda}{2\sqrt{Dt}\lambda}\Big)\Big)\Big)(\psi-1))+4be^{-\frac{d+h}{\lambda}}(-1+e^{h/\lambda})h\lambda\psi \\
& +e^{-\frac{d+h}{\lambda}}(-1+e^{h/\lambda})\lambda(1-\psi)\Bigg(\frac{4\sqrt{Dt}(1-e^{-\frac{h^2}{4Dt}})}{\sqrt{\pi}}+b\Big(\frac{4\sqrt{Dt}(-1+e^{-\frac{h^2}{4Dt}})}{\sqrt{\pi}}+2h\mathrm{erf}\Big(\frac{h}{2\sqrt{Dt}}\Big)\Big) \\
& +2h\mathrm{erfc}\Big(\frac{h}{2\sqrt{Dt}}\Big)\Bigg)\Bigg] \qquad \text{(F2)}
\end{aligned}
$$

Two dimensions, square FRAP:

$$
\begin{aligned}
f(t) \;=\;& \frac{C_0 e^{-\frac{d}{\lambda}}\lambda}{4h^2}(-4e^{-\frac{h}{\lambda}}(-1+e^{h/\lambda})h(\psi-1)+\frac{1}{\sqrt{\pi}}(2(b-1)e^{-\frac{(2Dt+h\lambda)^2}{4Dt\lambda^2}}(e^{\frac{h^2}{4Dt}}h\sqrt{\pi}\mathrm{erf}(\frac{h}{2\sqrt{Dt}})\\
&-2(-1+e^{\frac{h^2}{4Dt}})\sqrt{Dt})(e^{\frac{Dt}{\lambda^2}}(e^{h/\lambda}\mathrm{erf}(\frac{\sqrt{Dt}}{\lambda})+\mathrm{erf}(\frac{h\lambda-2Dt}{2\sqrt{Dt}\lambda}))-e^{h/\lambda}\mathrm{erf}(\frac{h}{2\sqrt{Dt}}))(\psi-1))\\
&-\frac{1}{\sqrt{\pi}}(2(b-1)e^{-\frac{h^2}{4Dt}-\frac{Dt}{\lambda^2}}(e^{\frac{h^2}{4Dt}}h\sqrt{\pi}\mathrm{erf}(\frac{h}{2\sqrt{Dt}})-2(-1+e^{\frac{h^2}{4Dt}})\sqrt{Dt})(-\mathrm{erf}(\frac{d}{\sqrt{Dt}})+\mathrm{erf}(\frac{2d+h}{2\sqrt{Dt}})\\
&+e^{\frac{Dt+2d\lambda}{\lambda^2}}(\mathrm{erf}(\frac{Dt+d\lambda}{\sqrt{Dt}\lambda})-e^{h/\lambda}\mathrm{erf}(\frac{2Dt+2d\lambda+h\lambda}{2\sqrt{Dt}\lambda})))(\psi-1))\\
&+\frac{1}{\sqrt{\pi}}(2(b-1)e^{-\frac{(2Dt+h\lambda)^2}{4Dt\lambda^2}}(e^{\frac{h^2}{4Dt}}h\sqrt{\pi}\mathrm{erf}(\frac{h}{2\sqrt{Dt}})-2(-1+e^{\frac{h^2}{4Dt}})\sqrt{Dt})(\mathrm{erf}(\frac{d+h}{\sqrt{Dt}})-\mathrm{erf}(\frac{2d+h}{2\sqrt{Dt}})\\
&+e^{\frac{Dt+2d\lambda+h\lambda}{\lambda^2}}(\mathrm{erf}(\frac{2Dt+2d\lambda+h\lambda}{2\sqrt{Dt}\lambda})-e^{h/\lambda}\mathrm{erf}(\frac{Dt+(d+h)\lambda}{\sqrt{Dt}\lambda})))(\psi-1))+4b(1-e^{-\frac{h}{\lambda}})h\psi\\
&+(b-1)e^{-\frac{h}{\lambda}}(-1+e^{h/\lambda})(1-\psi)(\frac{4\sqrt{Dt}(-1+e^{-\frac{h^2}{4Dt}})}{\sqrt{\pi}}+2h\mathrm{erf}(\frac{h}{2\sqrt{Dt}}))\\
&-(b-1)e^{-\frac{Dt+h\lambda}{\lambda^2}}(1-\psi)(\frac{4\sqrt{Dt}(-1+e^{-\frac{h^2}{4Dt}})}{\sqrt{\pi}}+2h\mathrm{erf}(\frac{h}{2\sqrt{Dt}}))(\mathrm{erf}(\frac{h}{2\sqrt{Dt}})\\
&+e^{\frac{Dt}{\lambda^2}}(e^{h/\lambda}\mathrm{erfc}(\frac{2Dt+h\lambda}{2\sqrt{Dt}\lambda})-\mathrm{erfc}(\frac{\sqrt{Dt}}{\lambda}))))
\end{aligned}
\tag{F3}
$$

$$
\begin{aligned}
f_{\mathrm{center}}(t) \;=\;& \frac{3C_0 e^{-\frac{d}{\lambda}}\lambda}{2h^2}(-2e^{-\frac{2h}{3\lambda}}(-1+e^{\frac{h}{3\lambda}})h(\psi-1)+\frac{1}{\sqrt{\pi}}((b-1)e^{-\frac{1}{9}h(\frac{h}{Dt}+\frac{6}{\lambda})}(-1+e^{\frac{h}{3\lambda}})(6\sqrt{Dt}(-1+e^{\frac{h^2}{12Dt}})\\
&+e^{\frac{h^2}{9Dt}}h\sqrt{\pi}\mathrm{erf}(\frac{h}{6\sqrt{Dt}})-2e^{\frac{h^2}{9Dt}}h\sqrt{\pi}\mathrm{erf}(\frac{h}{3\sqrt{Dt}}))(\psi-1))-\frac{1}{\sqrt{\pi}}((b-1)e^{-\frac{(3Dt+h\lambda)^2}{9Dt\lambda^2}}(6\sqrt{Dt}(-1+e^{\frac{h^2}{12Dt}})\\
&+e^{\frac{h^2}{9Dt}}h\sqrt{\pi}\mathrm{erf}(\frac{h}{6\sqrt{Dt}})-2e^{\frac{h^2}{9Dt}}h\sqrt{\pi}\mathrm{erf}(\frac{h}{3\sqrt{Dt}}))(e^{\frac{2h}{3\lambda}}\mathrm{erf}(\frac{h}{6\sqrt{Dt}})-e^{\frac{2h}{3\lambda}}\mathrm{erf}(\frac{h}{3\sqrt{Dt}})\\
&+e^{\frac{Dt}{\lambda^2}}(\mathrm{erf}(\frac{h\lambda-3Dt}{3\sqrt{Dt}\lambda})-e^{\frac{h}{3\lambda}}\mathrm{erf}(\frac{h\lambda-6Dt}{6\sqrt{Dt}\lambda})))(\psi-1))+\frac{1}{\sqrt{\pi}}((b-1)e^{-\frac{h^2}{9Dt}-\frac{Dt}{\lambda^2}}(6\sqrt{Dt}(-1+e^{\frac{h^2}{12Dt}})\\
&+e^{\frac{h^2}{9Dt}}h\sqrt{\pi}\mathrm{erf}(\frac{h}{6\sqrt{Dt}})-2e^{\frac{h^2}{9Dt}}h\sqrt{\pi}\mathrm{erf}(\frac{h}{3\sqrt{Dt}}))(\mathrm{erf}(\frac{3d+h}{3\sqrt{Dt}})-\mathrm{erf}(\frac{6d+h}{6\sqrt{Dt}})\\
&+e^{\frac{3Dt+6d\lambda+h\lambda}{3\lambda^2}}(\mathrm{erf}(\frac{6Dt+6d\lambda+h\lambda}{6\sqrt{Dt}\lambda})-e^{\frac{h}{3\lambda}}\mathrm{erf}(\frac{3Dt+3d\lambda+h\lambda}{3\sqrt{Dt}\lambda})))(\psi-1))+\\
&\frac{1}{\sqrt{\pi}}((b-1)e^{-\frac{h^2}{9Dt}-\frac{h}{\lambda}-\frac{Dt}{\lambda^2}}(6\sqrt{Dt}(-1+e^{\frac{h^2}{12Dt}})+e^{\frac{h^2}{9Dt}}h\sqrt{\pi}\mathrm{erf}(\frac{h}{6\sqrt{Dt}})\\
&-2e^{\frac{h^2}{9Dt}}h\sqrt{\pi}\mathrm{erf}(\frac{h}{3\sqrt{Dt}}))(\mathrm{erf}(\frac{3d+2h}{3\sqrt{Dt}})-\mathrm{erf}(\frac{6d+5h}{6\sqrt{Dt}})+e^{\frac{3Dt+6d\lambda+4h\lambda}{3\lambda^2}}(e^{\frac{h}{3\lambda}}\mathrm{erf}(\frac{6Dt+6d\lambda+5h\lambda}{6\sqrt{Dt}\lambda})\\
&-\mathrm{erf}(\frac{3Dt+3d\lambda+2h\lambda}{3\sqrt{Dt}\lambda})))(\psi-1))+\frac{1}{\sqrt{\pi}}((b-1)e^{-\frac{h^2}{9Dt}-\frac{h}{\lambda}-\frac{Dt}{\lambda^2}}(6\sqrt{Dt}(-1+e^{\frac{h^2}{12Dt}})\\
&+e^{\frac{h^2}{9Dt}}h\sqrt{\pi}\mathrm{erf}(\frac{h}{6\sqrt{Dt}})-2e^{\frac{h^2}{9Dt}}h\sqrt{\pi}\mathrm{erf}(\frac{h}{3\sqrt{Dt}}))(\mathrm{erf}(\frac{h}{6\sqrt{Dt}})-\mathrm{erf}(\frac{h}{3\sqrt{Dt}})\\
&+e^{\frac{3Dt+h\lambda}{3\lambda^2}}(\mathrm{erfc}(\frac{6Dt+h\lambda}{6\sqrt{Dt}\lambda})-e^{\frac{h}{3\lambda}}\mathrm{erfc}(\frac{3Dt+h\lambda}{3\sqrt{Dt}\lambda})))(\psi-1))+2be^{-\frac{2h}{3\lambda}}(-1+e^{\frac{h}{3\lambda}})h\psi)
\end{aligned}
\tag{F4}
$$

10. Supplementary references

1. E. V. Entchev, A. Schwabedissen, M. Gonzalez-Gaitan, *Cell* **103**, 981 (2000).
2. S. Pfeiffer, S. Ricardo, J.-B. Manneville, C. Alexandre, J.-P. Vincent, *Curr. Biol.* **12**, 957 (2002).
3. A. Charpilienne *et al.*, *J. Biol. Chem.* **276**, 29361 (2001).
4. M. Strigini, S. M. Cohen, *Curr. Biol.* **10**, 293 (2000).
5. M. Dundr, J. G. McNally, J. Cohen, T. Misteli, *J. Struct. Biol.* **140**, 92 (2002).
6. J. Rink, E. Ghigo, Y. Kalaidzidis, M. Zerial, *Cell* **122**, 735 (2005).
7. D. S. Sivia, C. J. Carlile, *J. Chem. Phys.* **96**, 170 (1992).
8. L. D. Landau, E. M. Lifshitz, *Fluid Mechanics* (Butterworth-Heineman, Boston, MA, ed. 2, 1987).
9. T. Bollenbach, K. Kruse, P. Pantazis, M. Gonzalez-Gaitan, F. Julicher, *Phys. Rev. Lett.* **94**, 018103 (2005).
10. A. Eldar, B.-Z. Shilo, N. Barkai, *Curr. Op. Gen. Dev.* **14**, 435 (2004).
11. T. Gregor, W. Bialek, R. R. d. R. van Steveninck, D. W. Tank, E. F. Wieschaus, *PNAS* **102**, 18403 (2005).
12. K. Kruse, P. Pantazis, T. Bollenbach, F. Julicher, M. Gonzalez-Gaitan, *Development* **131**, 4843 (2004).
13. A. D. Lander, Q. Nie, F. Y. Wan, **2**, 785 (2002).
14. D. Axelrod, D. E. Koppel, J. Schlessinger, E. Elson, W. W. Webb, *Biophys. J.* **16**, 1055 (1976).
15. R. R. Staples, M. Ramaswami, *J. Neurogen.* **13**, 119 (1999).
16. T. Y. Belenkaya *et al.*, *Cell* **119**, 231 (2004).
17. K. S. Krishnan *et al.*, *Neuron* **30**, 197 (2001).
18. T. Wucherpfennig, M. Wilsch-Brauninger, M. Gonzalez-Gaitan, *J. Cell Biol.* **161**, 609 (2003).

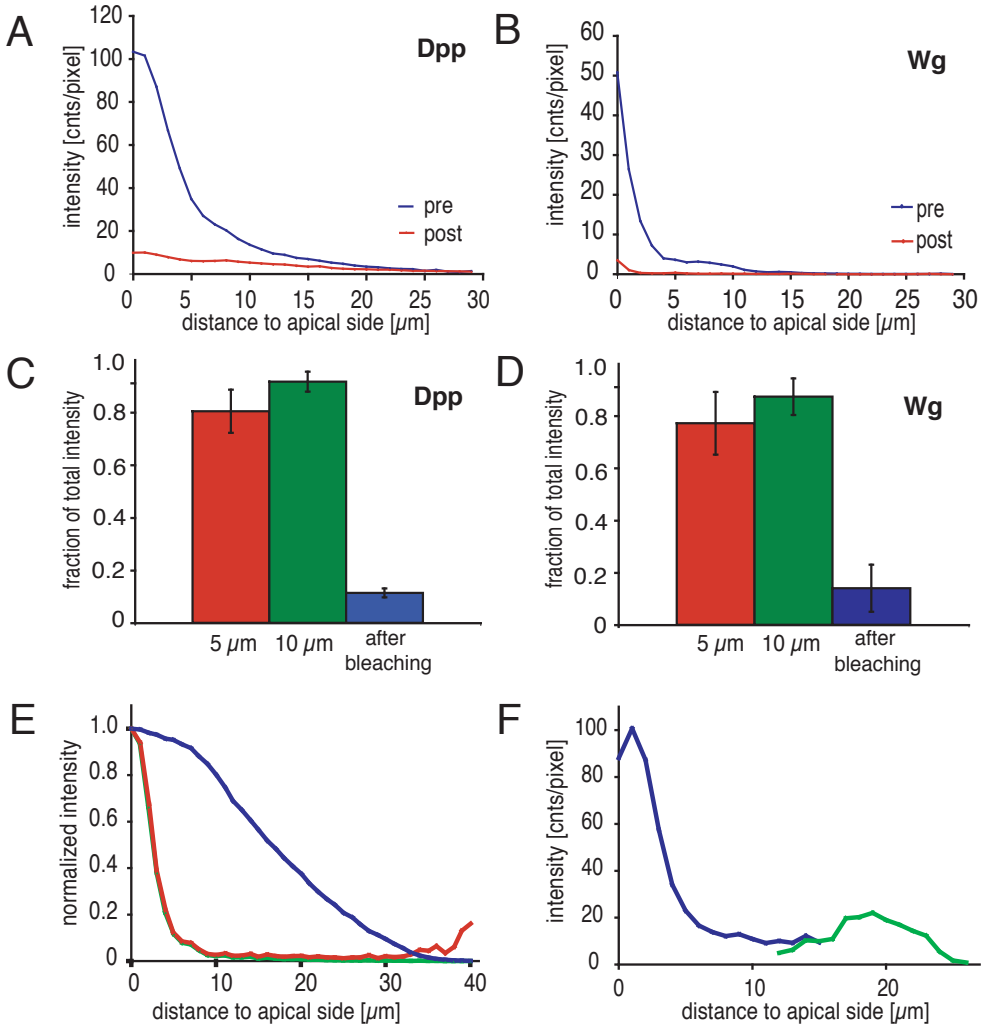

Supplementary figure S1. Apico-basal distribution of GFP-Dpp and GFP-Wingless and bleaching profile.

(A, B) A representative example of the apico-basal distribution of total GFP-Dpp (A) and GFP-Wingless (B) intensity in a 10 μm wide ROI adjacent to the source before bleaching (blue) and after bleaching (red). Intensity per 1 z-slice given. **(C,D)** Fractions of the total GFP-Dpp (C) and GFP-Wingless (D) intensity present in the most apical 5 μm (red), 10 μm (green), or remaining throughout the entire tissue depth after bleaching (blue). Total intensity has been measured in a 10 μm wide ROI adjacent to the source and normalized to 1. **(E)** Effect of decreasing light penetration on the apico-basal distribution of GFP-Dpp. Uniformly distributed cytosolic GFP was imaged to derive a "z-calibration" curve (blue). The apico-basal distribution of GFP-Dpp (green) was corrected for the penetration effect using the "z-calibration" curve, resulting in a new distribution (red). **(F)** Apico-basal distribution of intesities [cnts/pixel per 1 z-slice] of GFP-Dpp, produced by imaging a disc, embedded between two coverslips, from both the apical and the basal sides. The apico-basal z-stack is represented in blue and the inverted baso-apical z-stack in green. A small part of the overlap, used for concatenating the stacks, is shown.

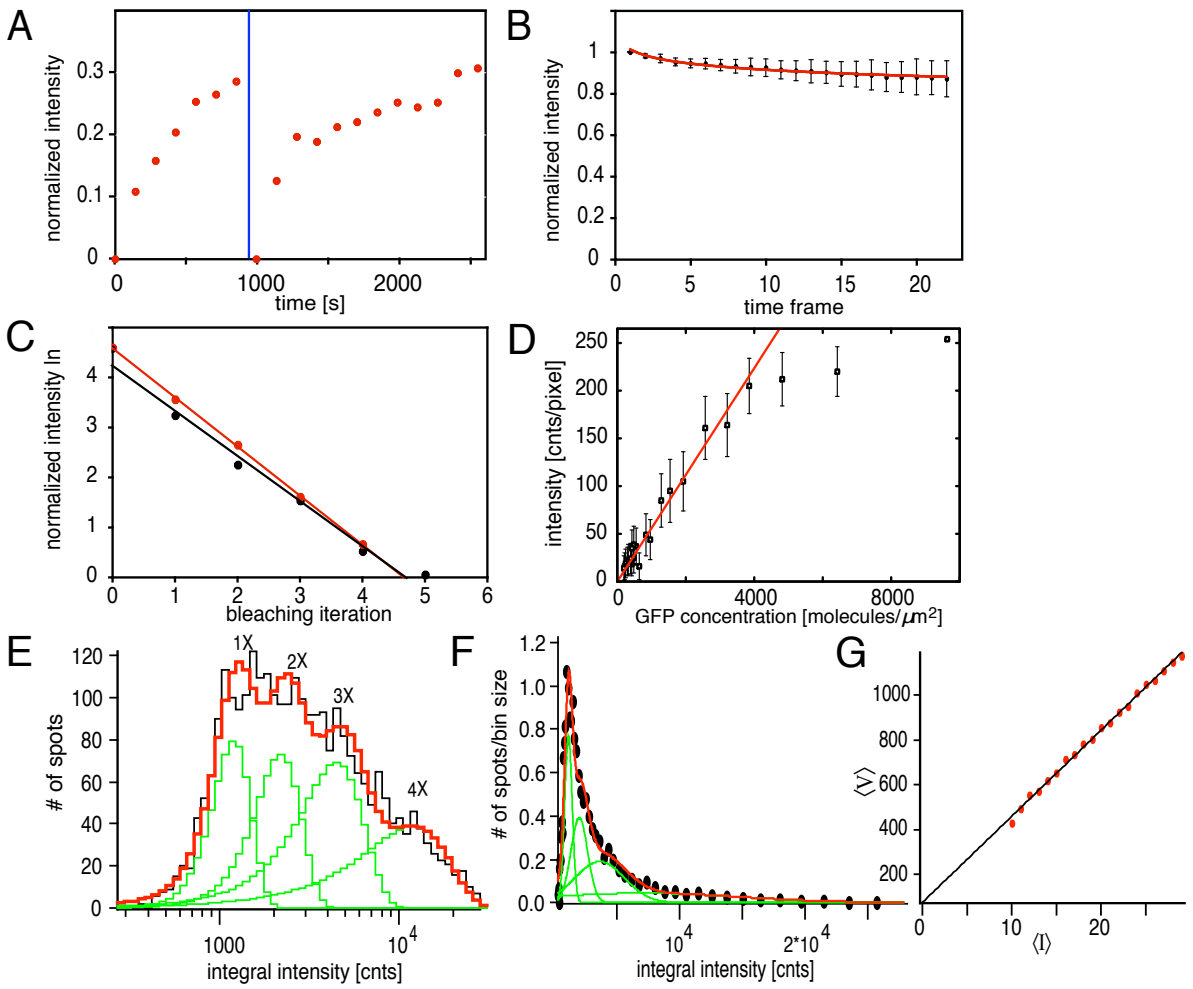

Supplementary figure S2. Imaging conditions in the FRAP experiments.
(A). Bleaching does not impair the ability of the tissue to recover. Bleaching in the ROI was performed as usual and the recovery was monitored for about 1000 s. The tissue was subsequently bleached again and the fluorescence was observed for another 1500 s. The recoveries seen after each bleaching are similar. The average fluorescence intensity in the ROI (blue dots) is normalized to 1 for the value before bleaching and 0 to the value immediately after bleaching. The blue line indicates the time of the second bleaching. **(B)** Bleaching in the course of imaging. Fixed GFP-Dpp was illuminated in the same conditions as in vivo 25 times. Average of 5 independent experiments is shown. Error bars are standard deviations and the fit is represented by a red line. Analogous GFP-Wingless experiments yield a similar result. **(C)** Stepwise bleaching assay for imaging in the linear range. The normalized fluorescence intensity logartithm of GFP-Dpp (black dots) and GFP-Wingless (red dots) is represented as a function of the bleaching iteration. A linear fit for GFP-Dpp and GFP-Wingless is represented by a line in the respective color . Two representative experiments are shown. **(D)** Calibration of fluorescence intensity to GFP concentration. GFP in solution at different concentrations was imaged under the same conditions as in the FRAP experiments (intensity per single z-section is given). Error bars represent standard deviations of 3 independent measurements for each concentration. A linear fit is represented by a red line. **(E-G)** Calibration of fluorescence intensity to GFP concentration using Rotavirus-like particles (VLPs), tagged with 120 GFP molecules each. A solution of VLPs was imaged in the same conditions as the FRAP assay. **(E)** The integral intensity distribution of the detected fluorescent structures is represented (black). In red is represented the fitted sum of 4 Gaussians (green). The first peak corresponds to a single virus (1X), the second to aggregates of two viruses (2X) and so on. **(F)** The integral intensity distribution from (E) has been divided by the bin size. This shows that the first single VLP peak is the major peak in the distribution. **(G)** Dependence of the variance of intensity measured in the vicinity of each pixel on the integral fluorescence intensity for low intensity values. The linear dependence is represented by a linear fit (black line).

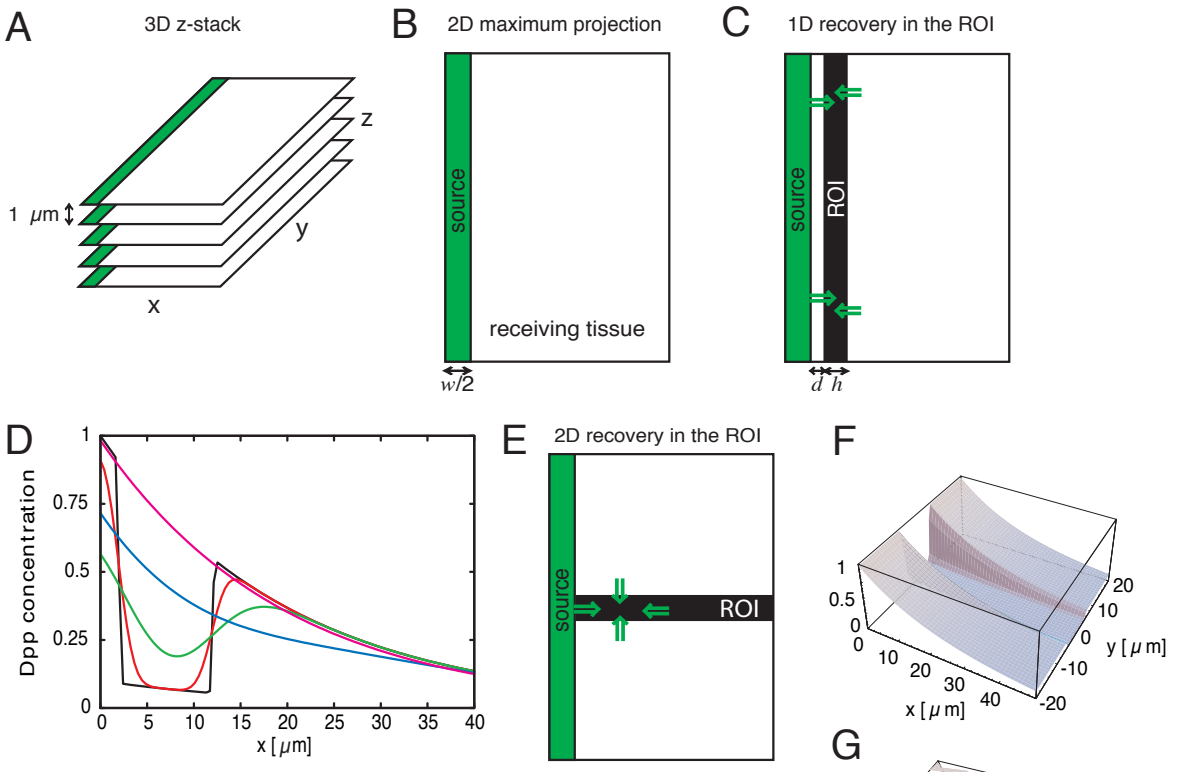

Supplementary figure S3. Data analysis.
(A) Schematic representation of the 5-section z-stack imaged at each time point in a FRAP assay. The overlapping optical sections are 1 μm apart. The optical slice thickness is 2.7 μm. Only the posterior compartment is depicted. The source is represented by a green stripe. Most of the fluorescence is localized in the most apical 5 μm, which are imaged (see Supplementary figure 1). **(B)** For each stack, a maximum projection is made, which allows treating the tissue as a two-dimensional structure. w is the width of the source and only half of the source is represented. **(C)** Geometry of "parallel" FRAP. The ROI (10 μm x 200 μm) is shown as a black stripe. d is the distance of the ROI to the source, and h is the width of the ROI. The recovery of fluorescence occurs mainly from the long sides of the ROI (green arrows) and is negligible from the short lateral sides of the ROI. This allows reducing the analysis of such FRAP experiments to one dimension. **(D)** Theoretical time development of the Dpp concentration profile in a "parallel" FRAP experiment. The different traces represent the concentration profiles at different time points after bleaching: black 0 s (immediately after bleaching); red 10 s; green 100 s; blue 1000 s; magenta 10000 s. The source is located at x=0. **(E)** Schematic representation of a "perpendicular" FRAP assay. Recovery in the ROI occurs from all directions in the tissue plane (green arrows), therefore two-dimensional data analysis is employed in this case. **(F-I)** Theoretical time development of the Dpp concentration profile in a "perpendicular" FRAP experiment. The different graphs (F-I) represent the concentration profiles at different time points after bleaching: (F) 1 s (immediately after bleaching); (G) 10 s; (H) 100 s; (I) 1000 s. The source is located at x=0.

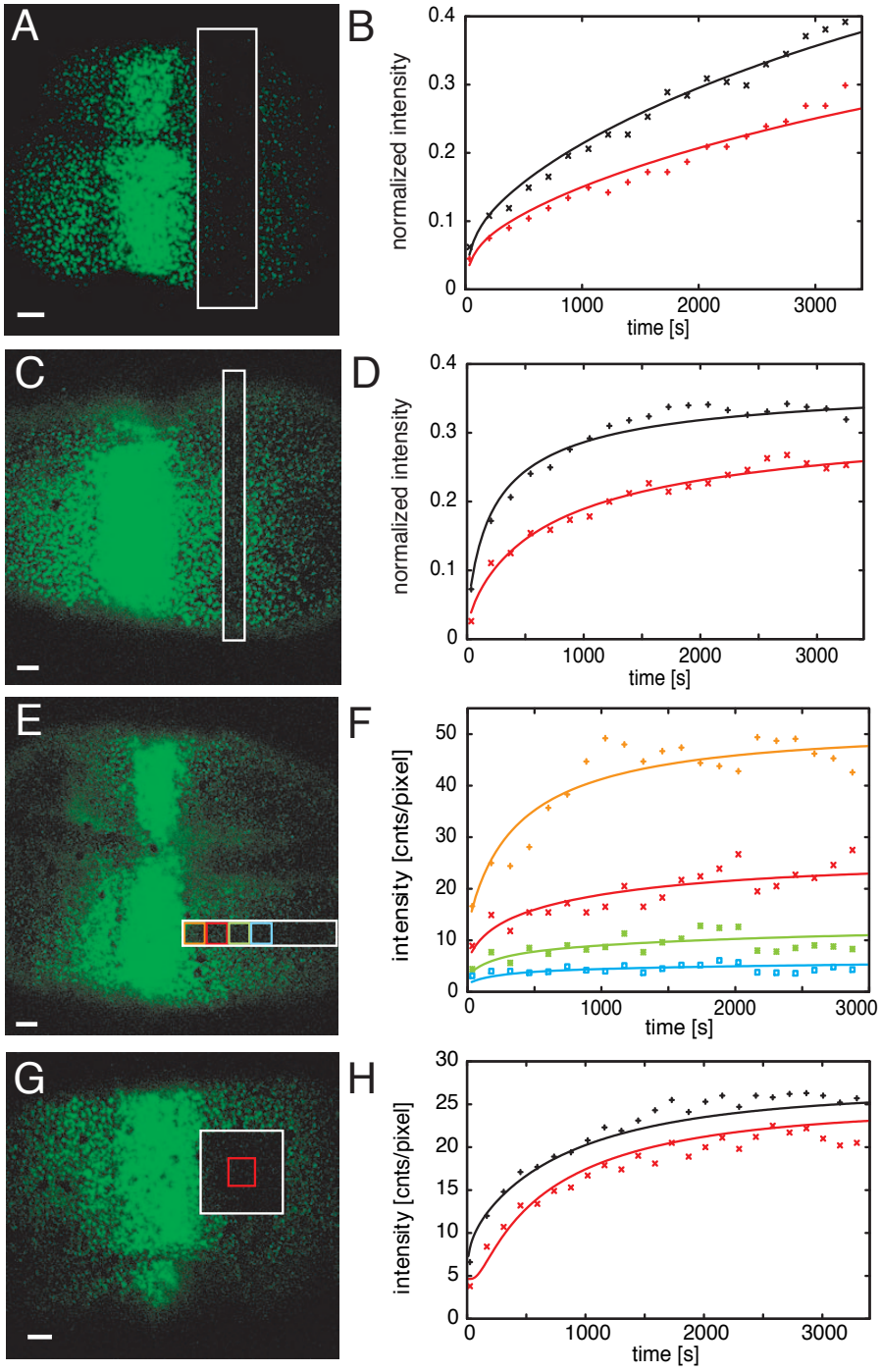

Supplementary figure S4. Modified FRAP assays. **(A)** A 20 μm wide stripe (white) of GFP-Dpp (green) at 25 ºC was bleached adjacent to the source. The recovery was analyzed using a one-dimensional model, with h=20 μm. Scale bar 10 μm. **(B)** Results of 2 independent experiments (red, black), in which a 20 μm wide stripe was bleached adjacent to the source. The average intensity in the ROI is normalized to 1 for the value before bleaching. **(C)** A 10 μm wide stripe (white) of GFP-Dpp at 25 ºC was bleached 20 μm away from the source. The recovery was analyzed using a one-dimensional model, with d=20 μm. Scale bar 10 μm. **(D)** Results of 2 independent experiments (red, black), in which a 10 μm wide stripe was bleached 20 μm away from the source. The average intensity in the ROI is normalized to 1 for the value before bleaching. **(E)** A 10 μm wide stripe (white) of GFP-Dpp at 25 ºC was bleached perpendicularly to the source. The recovery was analyzed with a two-dimensional model. The average intensity was measured over time in each 10 μm x 10 μm square (orange, red, green, blue). Scale bar 10 μm. **(F)** Two-dimensional analysis of one "perpendicular" FRAP experiment. The average fluorescence (of a maximum projection of 5 z-sections) in each square (orange, red, green, blue as in (E)) for each time point is represented as a dot, and the fits - as lines in the respective color. The theoretical curves for all squares are described by the same kinetic parameters, and only the geometric parameters of the ROI for each square are different. **(G)** A 30 μm x 30 μm square of GFP-Dpp was bleached next to the source. The recovery was analyzed using a two-dimensional model. The average intensity (of a maximum projection of 5 z-sections) was measured over time in the red 10 μm x 10 μm square in the center, and in the total ROI (white). Scale bar 10 μm. **(H)** Two-dimensional analysis of a 30 μm square experiment. The average fluorescence in the center ROI (red as in (G)) and in the total ROI (black) for each time point is represented as a dot, and the fits are represented as lines in the respective color. The theoretical curves for both squares are described by the same kinetic parameters, and only the geometric parameters of the ROI for each square are different.

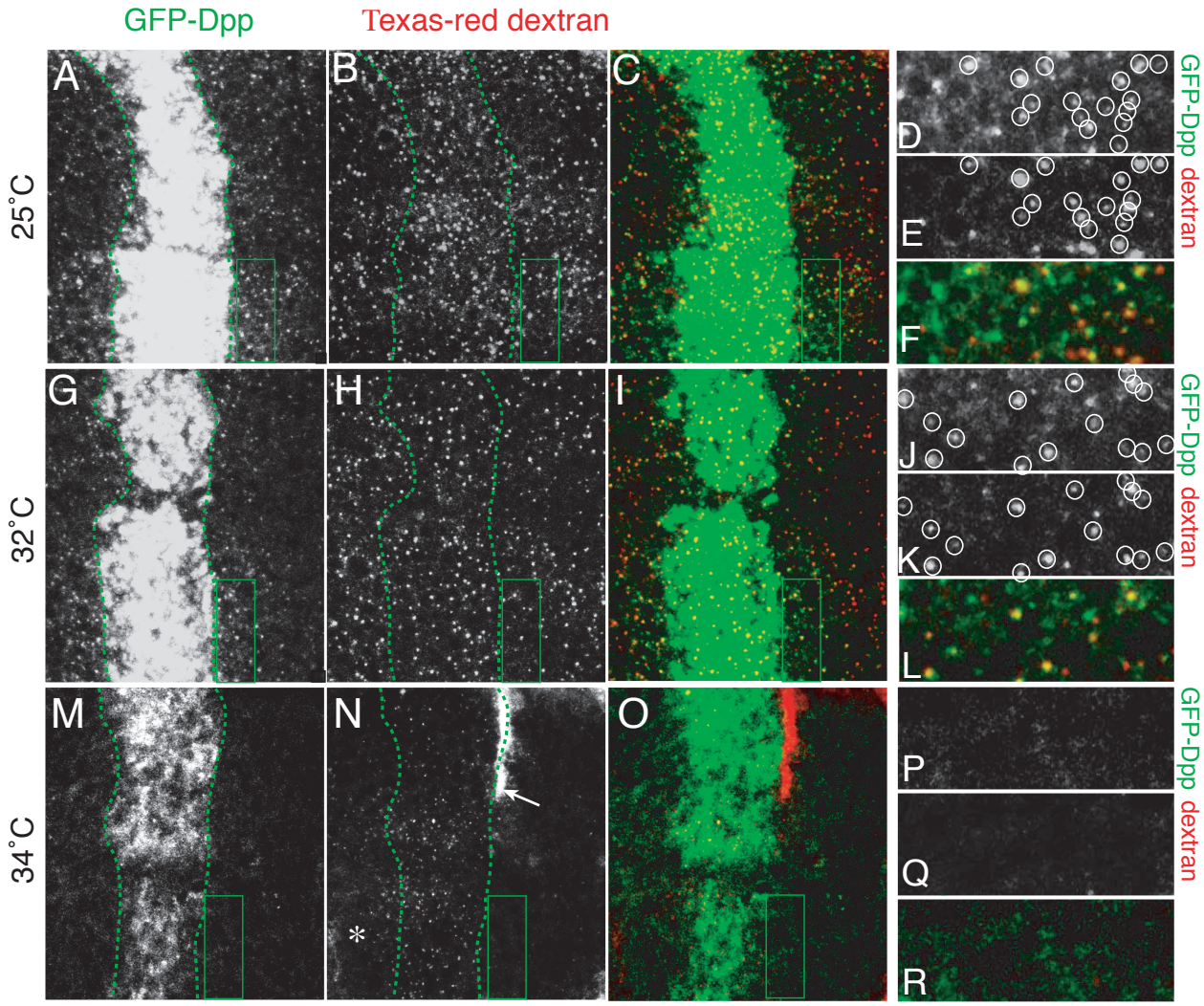

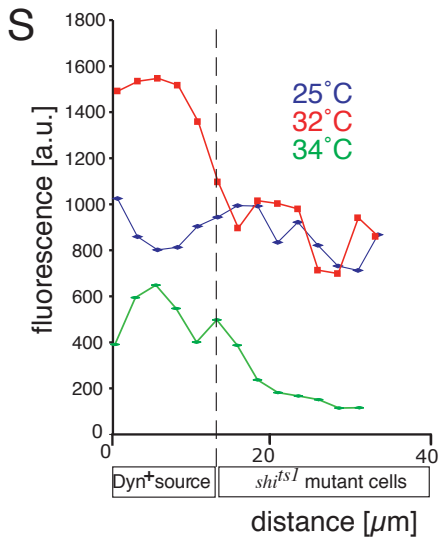

Supplementary figure S5. Temperature control of fluid phase and GFP-Dpp endocytosis in the "shibire rescue" experiment.

GFP-Dpp and Texas-red dextran (MW10000) internalized into endosomes upon a 20 minutes pulse after 6 hours at 25 ºC **(A-F)**, 32 ºC **(G-L)** and 34 ºC **(M-R)** in "shibire rescue" developing wings. **(A,D,G,J,M,P)** GFP-Dpp distribution. **(B,E,H,K,N,Q)** Texas-red dextran. **(C,F,I,L,O,R)** merge: GFP-Dpp (green) and Texas-red dextran (red). **(D-F, J-L, P-R)** high magnification of the respective boxed regions. **(S)** Quantification of Texas-red dextran fluorescence as a function of the position with respect to the Dynamin^{+} source of Dpp. Before the 6 hours treatment, larvae were kept at 25˚C. Higher levels of endocytosis in the *Dyn*$^{+}$ rescued cells at 25˚C could be due to overexpression of Dynamin at the permissive temperature (S). In **N**, arrow points to a fold which traps the Texas-Red dextran between the wildtype source and the shits receiving mutant cells which is frequently observed in this condition; asterisk, indicates internalization in the anterior compartment due to perdurance of gal4 as previously described in (Entchev et al., 2000). 3 confocal sections encompassing the top 5 microns of the epithelium are projected. Genotype: *shi^{ts}; UAS–Dynamin+/+;dpp–gal4/UAS-GFP-Dpp.*

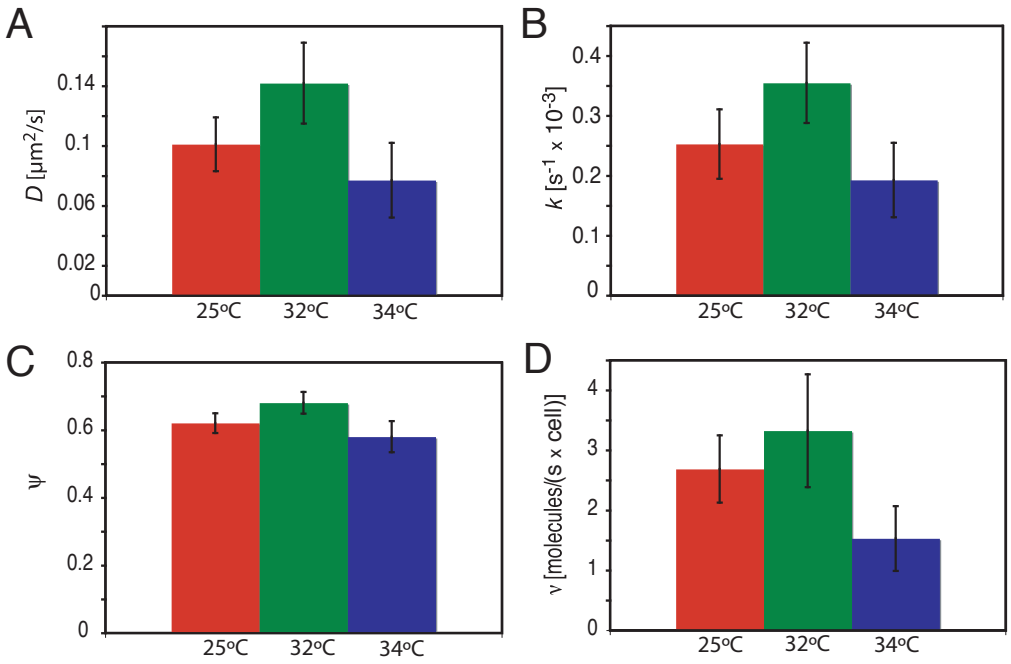

Supplementary figure S6. Temperature effect on GFP-Dpp kinetics.
(A-D) The average values from FRAP experiments with GFP-Dpp for D, k, ψ, and ν (A-D respectively) are represented for three different temperatures (25 ºC – red (n=8), 32 ºC – green (n=7), 34 ºC – blue (n=8)). Error bars are standard errors of the mean.

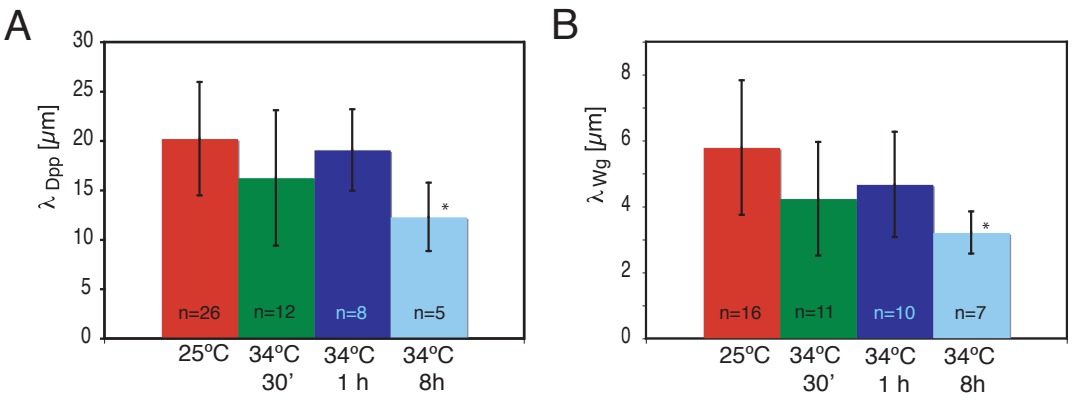

Supplementary figure S7. The decay length does not change after 1 hour at higher temperature.

(A, B) The average decay length for GFP-Dpp (A) and GFP-Wingless (B) is indicated for 25 ºC and 34 ºC (after 30 minutes, 1 hour and 8 or 9 hour incubation). The number of gradients analyzed in each case is indicated in the bars. Error bars are standard deviations. The asterisk indicates $p<0.05$ on a T-test comparing the value at 34 ºC to that at 25 ºC.

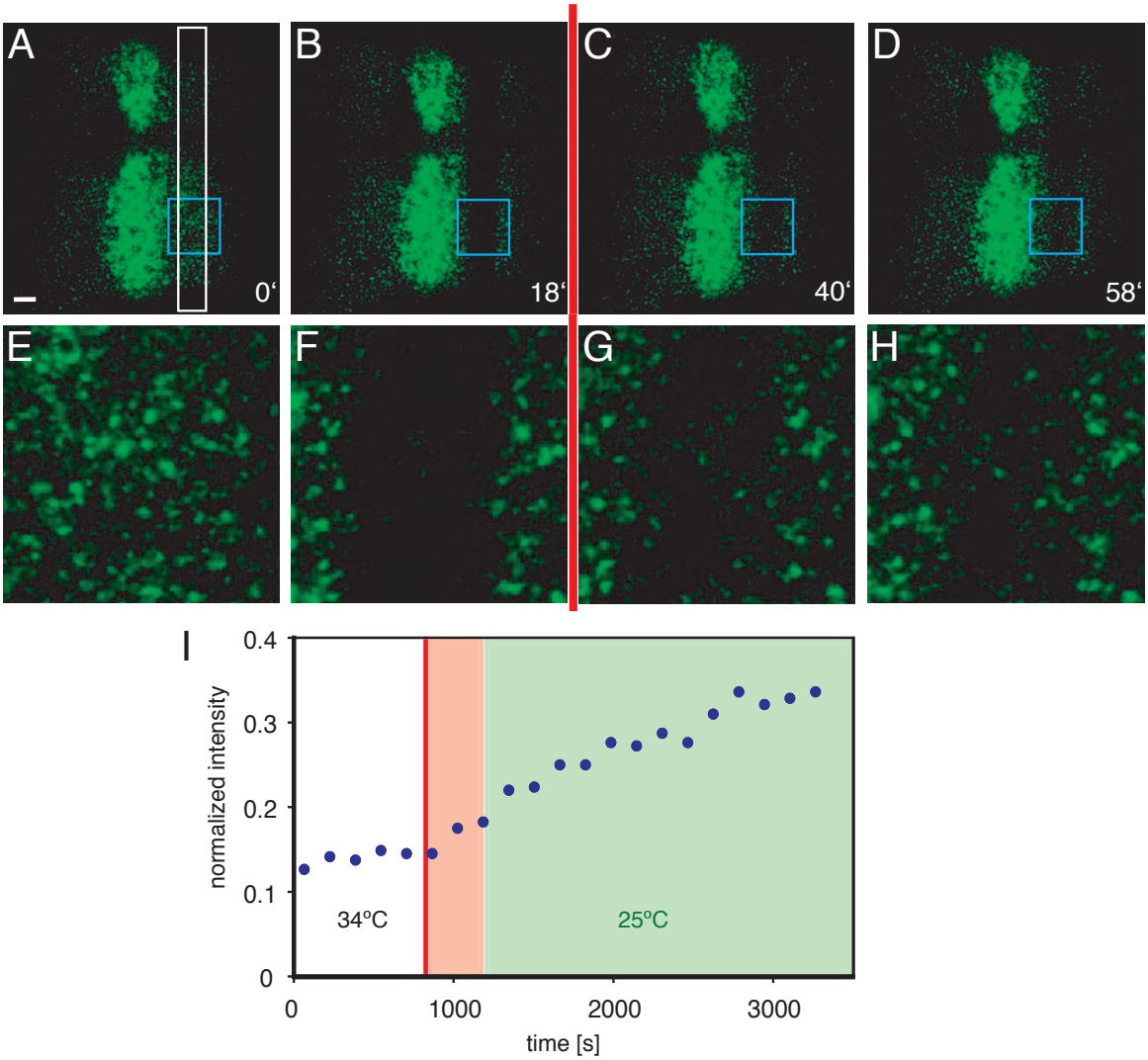

Supplementary figure S8. The block of endocytosis in “shibire rescue” experiments is reversible.

(A-D) Snapshots of a FRAP GFP-Dpp “shibire rescue” (green) experiment, where the temperature was kept at 34 ºC for the first 18 minutes and then shifted to 25 ºC. The temperature shift is indicated by a red line. Maximum projections of 5-section z-stacks are represented for each time point. Time in minutes is indicated in the bottom right corner of each snapshot. Scale bar 10 μm. (A) represents the image before bleaching. The ROI is outlined in white. The rectangle outlined in blue is magnified in **(E-H)** for each time point respectively. **(I)** Quantitative representation of a reversible GFP-Dpp “shibire rescue” FRAP experiment. The temperature shift is marked by a red line. The area marked in red indicates approximately the time of cooling the sample from 34 ºC to 25 ºC. The green area indicates the part of experiment performed at 25 ºC. The average fluorescence intensity in the ROI has been normalized to 1 for the value before bleaching.

experiment description		D [$\mu m^2/s$]	k [s^{-1}] x 10^{-4}	ψ	ν [molec./s·cell]	R^2	n
GFP-Dpp	**25 ºC**	0.10±0.05	2.52±1.29	0.62±0.08	2.69±1.58	0.95±0.03	8
	32 ºC	0.14±0.07	3.54±1.77	0.68±0.09	3.32±2.48	0.95±0.01	7
	34 ºC	0.08±0.07	1.92±1.76	0.58±0.13	1.53±1.52	0.93±0.05	8
GFP-Dpp "shi rescue"	**25 ºC**	0.12±0.09	3.05±2.32	0.60±0.17	2.58±2.04	0.91±0.05	11
	32 ºC	0.06±0.02	1.53±0.58	0.61±0.09	1.11±0.44	0.94±0.03	7
GFP-Dpp modified 25 ºC	**20 μm wide**	0.12±0.10	3.01±2.52	0.61±0.18	2.03±2.14	0.95±0.05	3
	20 μm away	0.07±0.05	1.55±1.20	0.35±0.03	5.18±0.34	0.95±0.03	2
	perpendicular FRAP	0.04±0.03	1.40±1.40	0.61±0.26	4.24±3.18	0.97±0.02	3
	30 μm square	0.11±0.05	2.86±1.32	0.62±0.16	6.30±1.57	0.95±0.01	2
GFP-Wingless	**25 ºC**	0.05±0.04	14.27±10.44	0.09±0.13	18.70±12.92	0.96±0.03	9
	34 ºC	0.04±0.04	11.84±12.15	0.38±0.27	18.19±17.45	0.95±0.04	9
GFP-Wingless "shi rescue"	**34 ºC**	0.26±0.20	7.13±5.71	0.28±0.29	10.04±17.67	0.95±0.02	10

Supplementary table S1. Summary of the kinetic parameters.
For all values the mean and the standard deviation are reported. The last column (n) contains the number of experiments considered for each experimental condition. R^2 values describe the agreement between the experimental data and the theoretical curves, used to derive the parameter values.

Kinetics of Morphogen Gradient Formation
Kicheva et al.

Supplementary video legends

Movie S1.
Movie showing a time-lapse FRAP experiment of GFP-Dpp at 25 ºC. Posterior, right. A 10 µm wide stripe is bleached adjacent to the source in the posterior compartment. The time in the bottom right corner indicates seconds after the start of the experiment. The image immediately before bleaching is shown at 0 seconds.

Movie S2.
Movie showing a time-lapse FRAP experiment of GFP-Dpp at 34 ºC in a shibire rescue. Posterior, right. A 10 µm wide stripe is bleached adjacent to the source in the posterior compartment. The time in the bottom right corner indicates seconds after the start of the experiment. The image immediately before bleaching is shown at 0 seconds.

Movie S3.
Movie showing a time-lapse FRAP experiment of GFP-Wingless at 25 ºC. Posterior, right. A 10 µm wide stripe is bleached adjacent to the source in the posterior compartment. The time in the bottom right corner indicates seconds after the start of the experiment. The image immediately before bleaching is shown at 0 seconds.